═══════════ **DIELECTRICS** ═══════════

Paramagnetic Mn Antisite Defects in Nanoceramics of Aluminum−Magnesium Spinel

A. F. Zatsepin^a, A. N. Kiryakov^{a,}*, D. R. Baytimirov^a, T. V. Dyachkova^b,
A. P. Tyutyunnik^b, and Yu. G. Zainulin^b

^{a} *Ural Federal University Named after the First President of Russia B.N. Yeltsin, Yekaterinburg, Russia*
^{b} *Institute of Solid State Chemistry, Ural Branch, Russian Academy of Sciences, Yekaterinburg, Russia*
**e-mail: arseny.kiriakov@urfu.tu*

Abstract—The effect of structure and size parameters on the formation of intrinsic and impurity paramagnetic centers in nanoceramics of aluminum−magnesium spinel is studied. The studied samples (grain size ~30 nm) are obtained by thermobaric synthesis. Microcrystalline ceramics and $MgAl_2O_4$ single crystal are used as the reference samples. Characteristic paramagnetic centers of Mn^{2+} (hyperfine structure constant (HFS) $A = 82$ G) are present in both single crystal and microceramics. In the studied samples of nanoceramics in the initial state, both impurity Mn^{2+} and intrinsic F^+ centers exist. Unlike the nanoceramics, the centers of F^+ type in the reference sample appear only after the irradiation with accelerated electrons (130 keV). The parameters of Mn^{2+} centers in nanoceramics significantly differ on that in microceramics and single crystal. EPR signal of Mn^{2+} centers in nanoceramics is characterized by two anomalous constant HFS ($A_1 = 91.21$ G, $A_2 = 87.83$ G) caused by two types of octahedrally coordinated manganese ions ($[Mn^{2+}]_{Al^{3+}}$ antisite defects). The features of spectral parameters of manganese centers correlate with a decrease in the cell parameter of $MgAl_2O_4$ in the nanostructural state. The observed effects are interpreted based on the assumed scheme of $[Mn^{2+}]_{Al^{3+}}$ charge compensation by the aluminum antisite defect and F^+ center.

Keywords: electron paramagnetic resonance, $MgAl_2O_4$, nanoceramics, microceramics, hyperfine structure, antisite defects

DOI: 10.1134/S1063783420010370

INTRODUCTION

Intense development of photonics and electronics requires the creation of new functional materials with specific properties such as high radioactive resistance, transparency in a wide spectral range, and thermal stability. The ceramics of aluminum−magnesium spinel is one of the most radiation-resistant materials, which is proved in many works on the irradiation of spinel with electrons, neutrons, and ions having different energies [1−7]. The spinel is also an attractive material for the doping with transition 3*d*-elements and rare-earth elements to obtain desired optical properties (absorption, luminescence) [8−11].

As a result of high-energy impact on the crystal structure of spinel (ion implantation, accelerated electrons, fast neutrons, thermobaric effects), both intrinsic and impurity defects with a local disturbance of the crystal field form. Clear representation of the effect of intrinsic and extrinsic defects on the matrix of aluminum-magnesium spinel is important for the understanding of the mechanisms of the formation of defects and their microscopic parameters.

As it is well known, the neutron or ionic bombardment of aluminum−magnesium spinel ($MgAl_2O_4$) stimulates the formation of anionic sublattice defects (VO) (V_O) [1−3]. Such anionic defects can be induced as a result of thermochemical reducing [12]. Anionic vacancies act as the effective electron traps. When one or two electrons are trapped by an anionic vacancy, partial or complete charge compensation occurs, and it is accompanied by the formation of F^+ and F centers, respectively. The trapping of one unpaired electron is characterized by band with a *g*-factor of ~2.003 in the electron paramagnetic resonance spectra [1]. The features of change in the EPR signal in a single crystal with the contribution of one F^+ center are described in details elsewhere [13]. However, the behavior of F^+ centers in the synthesized ceramics is poorly studied and needs a detailed consideration.

The cationic sublattice of spinel consists of two types of cations, which leads to the formation of two types of cationic sublattices: aluminum and magnesium. Aluminum and magnesium cations are in octahedral and tetrahedral oxygen surrounding, respec-

tively. Under a high-energy influence (neutron, electron, ionic radiation, thermobaric impact), the formation of the defects of cationic mixing (antisite defects, ADs) is possible between the two types of sublattices. Such defects are an aluminum ion in the manganese position $[Al^{3+}]_{Mg^{2+}}$ and vice versa. In this case, the charge compensation is carried out by the formation of a pair of such defects $[Al^{3+}]_{Mg^{2+}}$ and $[Mg^{2+}]_{Al^{3+}}$ so that the neutrality of the crystal lattice is, in general, kept [14]. In ceramics obtained by the thermobaric treatment, a great amount of antisite defects exist due to the quenching of the nonequilibrium state of the system under high pressure as a result of fast removal of the pressure and temperature [15, 16]. The studies of paramagnetic features of single-crystal aluminum-magnesium spinel (AMS) and ADs showed that such centers do not have a resonance absorption of electromagnetic energy in a magnetic field, but can significantly distort the signal of paramagnetic centers present nearby (for example, F^+ centers) [13]. The question about the role of intrinsic defects of anionic and cationic sublattices or impurity centers in the EPR spectrum of nanoceramics is still opened.

The impurity defects in spinel are most frequently presented by the ions of $3d$ elements, whose specific spectral features are caused by the unshielded $3d$ shell. Under the influence of different types of radiation, strong reducing agents, or large mechanical loads, the distortion of the local surrounding of $3d$ ion occurs in the matrix. As a result, the spectral characteristics of $3d$ ions change, which allows them to be used as crystal field indicators. For example, the introduction of impurity Mn^{2+} ions into the AMS matrix provides a set of characteristic lines of hyperfine splitting (HFS) in EPR spectra due to the interaction of the magnetic moment of an unpaired electron with a magnetic moment of the nucleus. Since the spin of the Mn^{2+} nucleus $I = 5/2$, the nucleus magnetic moment will have $2I + 1 = 6$ values under the effect of a magnetic field $\mathbf{H}$. Thus, the electron magnetic moment is affected by the six different values of $\mathbf{H}$. In such a field, the magnetic moment of the electron μ_S will have six possible values of energy. As a result, each electronic Zeeman-sublevel splits into six sublevels of hyperfine structure, $(2S + 1)$. Based on $(2I + 1) \times (2S + 1)$, the resulting amount of energy levels is 36. Using corresponding magnetic quantum numbers for electron spin M and nuclear spin m ($-S \leq M \leq S$, $-I \leq m \leq I$), there are five allowed electron spin transition for $\Delta M_S = \pm 1$; $\Delta m_I = 0$: $|5/2m\rangle \leftrightarrow |3/2m\rangle \leftrightarrow |1/2m\rangle$, $|-1/2m\rangle \leftrightarrow |-3/2m\rangle$, $|-3/2m\rangle \leftrightarrow |-5/2m\rangle$, and $|1/2m\rangle \leftrightarrow |-1/2m\rangle$. However, due to a strong angle dependence of the first four transitions in both powder samples and ceramics, only the $|1/2m\rangle \leftrightarrow |-1/2m\rangle$ transition can be registered [17].

It is well known that the constant of HFS lines of manganese is extremely sensitive to the lattice param-

eters [18]. One of the possible factors significantly affecting the AMS lattice parameters is the method of its preparation and the size of crystallites. Therefore, the study of Mn^{2+} EPR spectra in an HFS range in the matrix of spinel obtained by various synthesis methods allows a deeper understanding of fundamental features of the interaction of an impurity manganese ion with the matrix.

This work is aimed at the study of paramagnetic centers of intrinsic and impurity defects in micro- and nanomodifications of the AMS ceramics. The following issues have been solved: the obtaining of EPR spectra of nanoceramics and standard samples before and after irradiation by accelerated electrons (130 keV), studying of the characteristics of saturation of different EPR signals, and the analysis of the obtained results.

MATERIALS AND METHODS

The nanoceramics samples were obtained by the thermobaric quenching of the AMS nanopowder in the Institute of Solid State Chemistry UB RAS. The content of impurities of transition elements in the studied ceramics is within standards regulated by respective documents on magnesium and aluminum nitrates (GOST 11088-75 and GOST 3757-75, respectively). The data concerning synthesis regimes and sample characterization are described [19]. The microceramics with a trace amount of Mn^{2+} impurities are provided by Peter the Great St. Petersburg Polytechnic University. The $MgAl_2O_4$ natural single crystal with a Mn^{2+} impurity is provided by the Zavaritsky Institute of Geology and Geochemistry UB RAS.

The characterization of micro- and nanoceramics was performed using the X-ray diffraction (XRD) of powder in transmitted light. The measurements were carried out at room temperature using a STADI-P diffractometer with a linear mini CDD detector in 2θ range of $5°-120°$ (step $0.05°$) with CuK_α^1 radiation. Polycrystalline silicon ($a = 5.43075$ (5) Å) was used as the standard of measurements. The search and identification of impurity phases were carried out using an ICDD (USA, Release 2016) database. The lattice constant and values of microstresses of the spinel are specified by the Rietveld method based on XRD data and CSAS software [20, 21]. The results of the XRD analysis of micro- and nanoceramics are listed in Table 1. According to literature data [22], the value of the lattice constant for the sample of natural single-crystal is 8.089 Å.

EPR spectra were recorded using an ELEXSYS 580 spectrometer (Bruker) with a resonance frequency of 9.87 GHz (X-band) at room temperature. The signal of quartz test-tube (Bruker) was taken into consideration. The EPR signal was normalized by the sample mass.

The irradiation with accelerated electrons was performed using a RADAN-EKSPERT pulse linear accelerator with the electron energy of 130 keV and a current density of 60 A/cm^2. The pulse duration was 1 ns; the fluence was ~2.4×10^{11} m^{-3}.

RESULTS

The EPR signal of nanoceramics and reference samples is given in Fig. 1. In all samples, the signal of hyperfine structure (HFS) of Mn^{2+} ions is registered. The highest amplitude of the HFS signal is observed for the natural crystal, which is explained by a higher concentration of impurity manganese and low defectively of the sample.

The position of HFS lines of the impurity Mn^{2+} in the sample of microceramics coincides with the position of these lines in the natural single-crystal. The couples forbidden transition lines are observed between the lines of hyperfine structure [17]. Additional bands are not observed in the EPR spectra of reference samples in the studied range. However, additional absorption lines with $g = 2.005$ and $g = 1.981$ are observed in nanoceramics spectra; their positions are characteristic for the F$^+$ centers and Ti^{3+} impurities [2, 23]. As it is seen from the EPR spectrum of nanoceramics, the impurity Mn^{2+} ions have the HFS constant increased in 10 G.

Figure 2 presents a detailed analysis of the edge HFS band. It is seen that the HFS signal is the superposition of at least two signals of [Mn^{2+}]$_{\text{Al}^{3+}}$ (1) and [Mn^{2+}]$_{\text{Al}^{3+}}$ (2). An average value of the HFS constant (parameter A) is 91.21 and 87.83 G for A_1 and A_2, respectively. Since the HFS bands located closer to the center have a lower difference of overlapping signals,

Table 1. Structural characteristics of the studied samples

Sample	Lattice constant a, Å	Coherent scattering region (CSR), nm	Microstresses
Nanoceramics	8.0844(1)	30(2)	0.00092
Microceramics	8.0856(1)	180(5)	0.00013

their separation is possible with a large error. Only the first and sixth components of the hyperfine structure were used for the calculation on A_1 and A_2.

The effect of the electron irradiation with the energy of 130 keV on the EPR signal is given in Fig. 3.

The appearance of an additional signal with g-factors of 2.007, 2.007, and 2.005 for the single crystal, micro- and nanoceramics, respectively, is registered in the samples. Decreasing the amplitude of HFS bands of Mn^{2+} is observed in all samples. The appearance of a broad signal with $g = 2.023$ is an additional feature of the EPR spectra of micro- and nanoceramics. The HFS parameters of reference samples and AMS nanoceramics before and after the irradiation with electrons are given in Table 2. It is seen that the irradiation with accelerated electrons leads to the decline of the amplitude of the HFS signal of Mn^{2+}; the sample of natural single-crystal is more sensitive to the irradiation. The change in g-factor and a slight change in the A parameter are also registered. No changes in the half-widths of the HFS lines (ΔH) were observed.

In order to estimate the observed changes in the absorption band of Mn^{2+} ion between single crystal sample and nanoceramics, the EPR HFS spectra on Mn^{2+} were recorded at different power of electromagnetic radiation. Figure 4 demonstrates the curves of
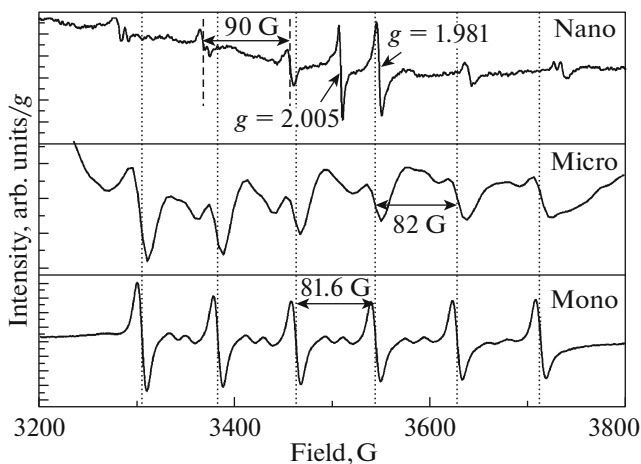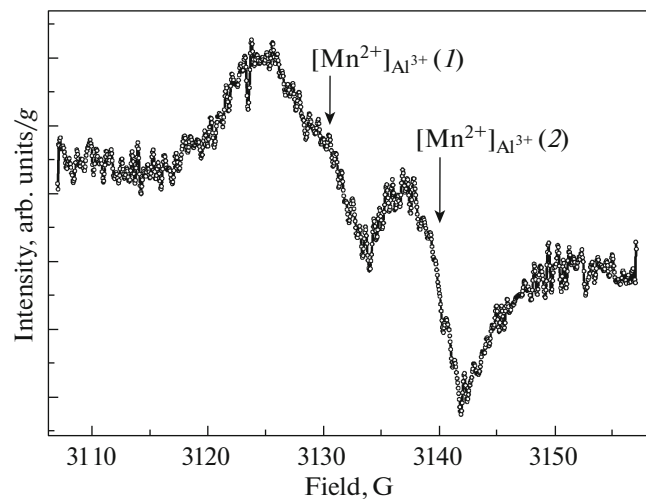

Fig. 1. EPR spectra of single-crystal sample (Mono), microceramics (Micro), and nanoceramics (Nano) of AMS. The dashed lines show the bands characteristic of the HFS of the Mn^{2+} ion in a single-crystal.

Fig. 2. The first component of the HFS of Mn^{2+} impurity in nanoceramics. The presence of two signals forming a band of a hyperfine structure is shown.
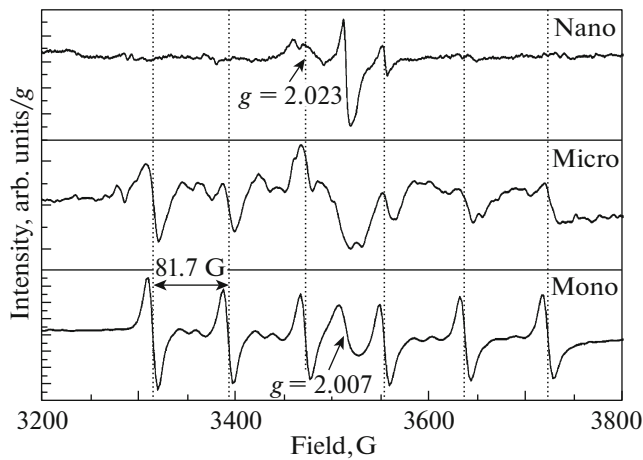
Fig. 3. EPR spectra of a single-crystal sample (Mono), microceramics (Micro), and nanoceramics (Nano) of AMS after irradiation with accelerated electrons. Dashed lines show the characteristic HFS bands of the Mn^{2+} ion.

Fig. 4. Dependence of the EPR signals of single-crystal HFS on the power of microwave radiation.

the dependence of the intensity of Mn^{2+} HFS components of the single crystal on the power of microwave radiation. The saturation of the allowed HFS transitions of Mn^{2+} in the single crystal occurs at 15 mW. Due to the fact that in the nanoceramics the HFS band of Mn^{2+} ion is formed by two signals, two characteristic power of saturation were determined for $[Mn^{2+}]_{Al^{3+}}$ (*1*) and $[Mn^{2+}]_{Al^{3+}}$ (*2*); their values were 32 and 2.6 mW, respectively (Fig. 5). This allows us to conclude that the observed signals relate to different centers. The character of the dependence of the saturation curve of the band with $g = 1.981$ in nanoceramics coincides with the Mn^{2+} band in the single-crystal, which indicates that a part of the signal is connected with the Mn^{2+} hyperfine structure. Apparently, the signal overlapping occurs in the nanoceramics at the mentioned *g*-factor. According to our estimates, the saturation of the signal of F^+ centers occurs at 100 mW. The bands of forbidden transitions of the single crystal sample demonstrate a minimum on a curve of the dependence of intensity on the power of the e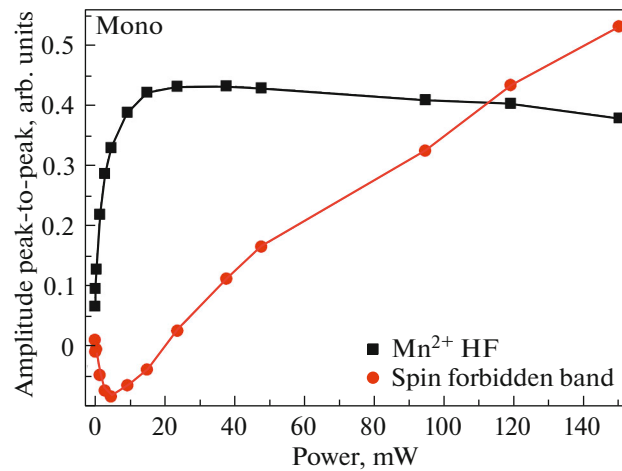lectromagnetic field at 5 mW. Further increasing of power leads to linear growth of the intensity of spin-forbidden transitions.

DISCUSSION

We showed earlier [24, 25] that the bands characteristic for F and F^+ centers are registered in the spectra of optical absorption of electronically bombed transparent micro- and nanoceramics. Microceramics was obtained by the method of uniaxial hot pressing in a graphite mold, which likely caused the appearance of anion vacancies according to the mechanism of thermochemical coloring [26]. As a result of the following irradiation with electrons (130 keV), their localization on the anionic vacancies takes place. The EPR signal of F^+ centers is registered in the initial samples of nanoceramics. The existence of anionic defects in nanoceramics is explained by a small size of crystallites and, as a consequence, a large number of grain boundaries. Such boundaries are the structure defects with the broken bonds including oxygen vacancies. High pressures stimulate the plastic deformation of grains, which leads to the breaking of chemical boundaries followed by the electron emitting. The localization of electron on anionic vacancy results in the formation of an F^+ center in the spinel nanoceramics.

Table 2. HFS parameters of Mn^{2+} ion in single-crystal, micro- and nanoceramics of AMS

Object	g-factor		HFS constant, G		Amplitude (arb. units/g)	
Sample	initial samples	after electron irradiation	initial samples	after electron irradiation	initial samples	after electron irradiation
Nanoceramics	2.0062	2.0081	91.37	90.9	11.8	8
Microceramics	2.0059	2.0064	82.0	82.6	5	4.6
Natural singlecrystal	2.0054	2.0080	81.6	81.7	1181.7	554.5
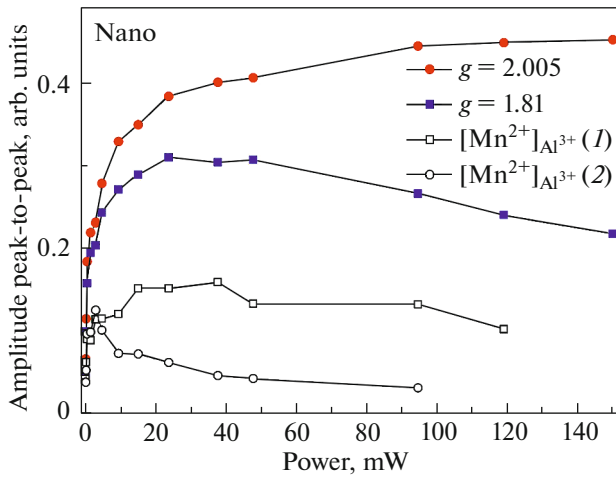
Fig. 5. Dependence of the EPR signals of nanoceramics on the power of microwave radiation.

Fig. 6. Hyperfine splitting constant A in impurity Mn^{2+} as a function of the covalency parameter c/n [18]. Asterisks and triangles show the values of the Mn^{2+} centers in nanoceramics and $MgAl_2O_4$ single-crystal, respectively [18].

Thus, the high-energy impact on the spinel matrix can be simulated by the thermobaric synthesis.

Decreasing the HFS amplitude in the EPR spectrum of Mn^{2+} after the irradiation with accelerated electrons correlates with the growth of the signal of F^+ centers. The authors of [13] showed that the formation of complex defects (with the participation of both an F^+ center and antisite defects) is possible in the spinel. However, the mechanism of the reaction of F^+ center with an impurity Mn^{2+} is unclear. It is possible that at a close location of F^+ centers to the Mn^{2+}, the wave functions of the electron localized on F^+ center and Mn^{2+} unpaired electron could overlap.

The saturation curves allow us not only to resolve the overlapping EPR signals, but estimate the time of spin–lattice (T_1) and spin–spin (T_2) relaxation. The method of T_1 and T_2 calculation is given in [27]. According to the calculations, the relaxation times of F^+ center in nanoceramics are $T_1 = 4.41 \times 10^{-4}$ s and $T_2 = 1.09 \times 10^{-8}$ s.

It is seen from Table 2 that a slight shift of the position of g-factor of the HFS occurs depending on the modification of the crystalline lattice (nano, micro, or mono). The change in the g-factor of Mn^{2+} HFS between the samples with the different structural state is connected with different concentration of intrinsic defects in the anionic and cationic sublattices. It is shown in [28] that the shrinkage of the spinel matrix leads to the growth of the defects of cationic sublattices (antisite defects). In our case, a strong nonequilibrium state of the system with a large amount of the antisite defects keeps in the nanoceramics sample due to the harding (a sharp decrease of pressure and temperature). Thus, in our opinion, the observed shift of the g-factor of the EPR signal of HFS of Mn^{2+} impurity is
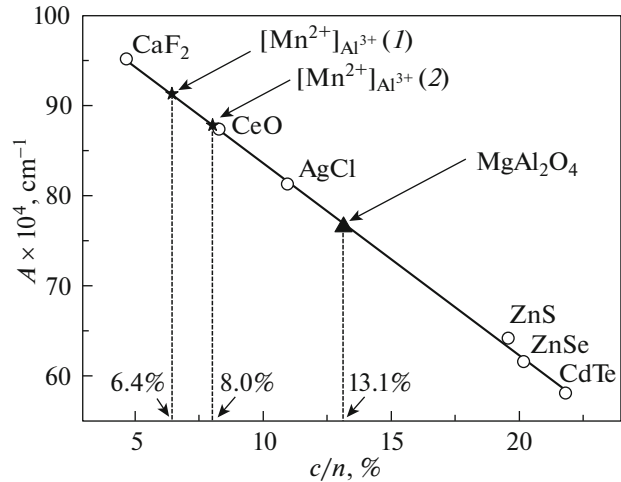
caused by a large concentration of the intrinsic defect of the matrix.

It is known that the HFS constant in the EPR spectrum of the impurity Mn^{2+} depends on the fractions of covalent bonding of manganese, i.e., on the degree of localization of the electron on the nucleus. When the fraction of the covalent bond decreases, the A parameter increases, for example, CdTe: $A = 55 \times 10^4$ cm^{-1}; ZnS: $A = 64 \times 10^4$ cm^{-1}; MgO: $A = 81 \times 10^4$ cm^{-1}; CaF$_2$: $A = 96 \times 10^4$ cm^{-1} [18]. Figure 6 demonstrates the given in [18] dependence of A parameter on c/n ratio, where c is a covalence degree taken from the expression of the difference of electronegativity of the transition metal impurity and its ligand and n is a number of ligands. Based on this dependence, the graphical estimation of the covalence parameter of the $[Mn^{2+}]_{Al^{3+}}$ (*1*) and $[Mn^{2+}]_{Al^{3+}}$ (*2*) paramagnetic centers in nanoceramics was conducted, and the values were 6.4 and 8.0%, respectively. Using the found values of the covalency parameter, the number of ligands can be refined by the empirical formula (1) [30]:

$$c = 1 - 0.16(X_A - X_B) - 0.035(X_A - X_B)^2, \quad (1)$$

where X_A and X_B are electronegativities of the anion and cation, respectively. In the case of the $MgAl_2O_4$ ideal single-crystal (without impurities or structural defects [18]), the amount of ligands is 4 (with a small error). For the $[Mn^{2+}]_{Al^{3+}}$ (*1*) and $[Mn^{2+}]_{Al^{3+}}$ (*2*) centers the n value is ~6. According to [30], the increase in the A parameter could be caused by the growth of the coordination number of impurity manganese.

Apparently, the additional shrinking of the lattice and existence of the significant fraction of antisite defects in the nanoceramics leads to the location of
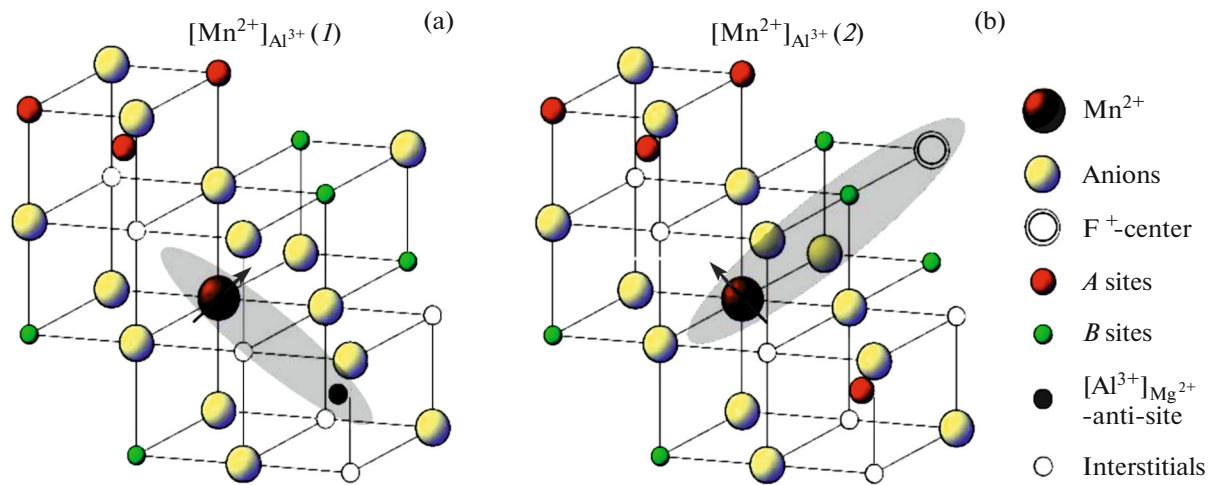
Fig. 7. Scheme of charge compensation of impurity Mn^{2+} with the participation of antisite defect (a) and F^+ center (b). The direction of interaction is indicated by the gray color.

impurity Mn^{2+} primary in octahedral positions. As a result, the unpaired electron is mostly localized on the Mn^{2+} nucleus.

The presence of two paramagnetic signals of $[Mn^{2+}]_{Al^{3+}}$ (*1*) and $[Mn^{2+}]_{Al^{3+}}$ (*2*) indicates two manganese ions with the different local surrounding. Since the number of ligands of such centers is a multiple of six, it is reasonable to assume the compensation of the missing positive charge in the node through the second coordination sphere. One of the more possible mechanisms of the charge compensation is the localization of the antisite defect (Fig. 7a). In this case, the charge of $[Mn^{2+}]_{Al^{3+}}$ ion is compensated by the $[Al^{3+}]_{Mg^{2+}}$ one. We consider the participation of F^+ centers as an alternative mechanism of the charge compensation of the impurity Mn^{2+} in the nanoceramics. Such a center could act as the charge compensator of the octahedral Mn^{2+} in the second coordination sphere (Fig. 7b).

Thus, the observed Mn^{2+} (*1*) and Mn^{2+} (*2*) signals (Fig. 2) are the results of the existence of two octahedral Mn^{2+} ions with the different surrounding. Moreover, because the value of the *A* parameter is higher for $[Mn^{2+}]_{Al^{3+}}$ (*1*), the charge compensation is possibly realized with the participation of the antisite defect. In this regard, in low concentrations the impurity Mn^{2+} acts as an indicator of the structural state of the regular and irregular (antisite) positions of Mg^{2+} cation in the nanoceramics.

CONCLUSIONS

The study of the paramagnetic centers of aluminum−magnesium spinel in the nanoceramics and its microceramic analog shows that the parameters of the

impurity and intrinsic centers of the microceramics are close to the single crystal. It allows us to conclude that, in this case, the grain with a large size can be considered as individual microscopic single-crystals. In nanoceramics, additional lattice distortions appear due to small grain size and synthesis features (thermobaric synthesis) which leads to the anomalous parameters of intrinsic and impurity centers such as F^+ and Mn^{2+} centers. The following specific examples can be highlighted:

1. It is established that the initial nanoceramics contains a significant part of F^+ centers with $g = 2.005$. After the electron irradiation, the amplitude of the specified signal increases and the appearance of a broad signal of unknown nature with $g = 2.023$ is observed. The characteristic times of spin−spin and spin−lattice relaxation of the F^+ center are 1.09×10^{-8} and 4.41×10^{-4} s, respectively.

2. An anomalous constant of the HFS of impurity Mn^{2+} was found, associated with six-fold coordination with respect to oxygen. Features of spectroscopic parameters of HFS of manganese centers correlate with a decrease in the lattice parameter in the nanostructured state.

3. The HFS signals with $A_1 = 91.21$ G and $A_2 = 87.83$ G arise due to the charge compensation of Mn^{2+} impurity with the participation of the antisite defect $[Al^{3+}]_{Mg^{2+}}$ and the F^+ center, respectively.

The set of the obtained results allows us to conclude that the method of ceramics synthesis significantly affects the structural properties giving the opportunity to manage those at the microlevel. The results of the study of the EPR spectra in the range of HFS of Mn^{2+} in the spinel matrix obtained by various

synthesis methods are of interest for the simulation of local interactions of impurity Mn^{2+} with the matrix.

CONFLICT OF INTEREST

REFERENCES

1. J. M. Costantini, G. Lelong, M. Guillaumet, W. J. Weber, S. Takaki, and K. Yasuda, J. Phys.: Condens. Matter **28**, 325901 (2016).

2. A. Ibarra, D. Bravo, M. A. Garcia, J. Llopis, F. J. Lopez, and F. Garner, J. Nucl. Mater. **258**, 1902 (1998).

3. G. P. Summers, G. S. White, K. H. Lee, and J. H. Crawford, Jr., Phys. Rev. B **21**, 2578 (1980).

4. Yu. Kazarinov, V. Kvatchadze, V. Gritsina, M. Abramishvili, Z. Akkhvledianni, M. Galustashvili, G. Dekanozishvili, T. Kalabegishvili, and T. Tavkelidze, Vopr. At. Nauki Tekh., No. 5, 8 (2017).

5. I. V. Afanasyev-Charkin, D. W. Cooke, V. T. Gritsyna, M. Ishimaru, and K. Sickafus, Vacuum **58**, 2 (2000).

6. M. Ishimaru, Y. Hirotsu, I. V. Afanasyev-Charkin, and K. E. Sickafus, J. Phys.: Condens. Matter **14**, 1237 (2002).

7. M. Ishimaru, Y. Hirotsu, and K. E. Sickafus, Microscopy **51**, 219 (2002).

8. N. Kishimoto, Y. Takeda, N. Umeda, V. T. Gritsyna, C. G. Lee, and T. Saito, Nucl. Instrum. Methods Phys. Res. B **166**, 840 (2000).

9. E. Hanamura, Y. Kawabe, H. Takashima, T. Sato, and A. Tomita, J. Nonlin. Opt. Phys. Mater. **12**, 467 (2003).

10. V. T. Gritsyna, V. A. Kobyakov, and L. A. Litvinov, J. Appl. Spectrosc. **45**, 837 (1986).

11. D. Valiev, S. Stepanov, O. Khasanov, E. Dvilis, E. Polisadova, and V. Paygin, Opt. Mater. **91**, 396 (2019).

12. S. Sawai and T. Uchino, J. Appl. Phys. **112**, 103523 (2012).

13. A. Lushchik, S. Dolgov, E. Feldbach, R. Pareja, A. I. Popov, E. Shablonin, and V. Seeman, Nucl. Instrum. Methods Phys. Res., Sect. B **435**, 31 (2018).

14. A. Navrotsky and O. J. Kleppa, J. Inorg. Nucl. Chem. **29**, 2701 (1967).

15. V. D'Ippolito, G. B. Andreozzi, D. Bersani, and P. P. Lottici, J. Raman Spectrosc. **46**, 1255 (2015).

16. Y. Zou, D. He, X. Wei, R. Yu, T. Lu, X. Chang, S. Wang, and L. Lei, Mater. Chem. Phys. **123**, 529 (2010).

17. J. S. Shaffer, H. A. Farach, and C. P. Poole, Jr., Phys. Rev. B **13**, 1869 (1976).

18. E. Simanek and K. A. Mueller, Chem. Phys. Lett. **4**, 482 (1970).

19. A. N. Kiryakov, A. F. Zatsepin, T. V. Dyachkova, A. P. Tytunyunnik, Y. G. Zainulin, G. Yakovlev, V. A. Pustovarov, and D. Bautimirov, IOP Conf. Ser.: Mater. Sci. Eng. **443**, 012014 (2018).

20. B. H. Toby, J. Appl. Crystallogr. **34**, 210 (2001).

21. A. C. Larson and R. B. von Dreele, Report LAUR No. 86 (1994).

22. H. Maekawa, S. Kato, K. Kawamura, and T. Yokokawa, Am. Mineral. **82**, 1125 (1997).

23. P. Lombard, B. Boizot, N. Ollier, A. Jouini, and A. Yoshikawa, J. Cryst. Growth **311**, 899 (2009).

24. A. N. Kiryakov, A. F. Zatsepin, Y. V. Shchapova, E. V. Golyeva, and V. A. Pustovarov, KnE Mater. Sci. **4**, 98 (2018).

25. A. N. Kiryakov, A. F. Zatsepin, A. I. Slesarev, T. V. Dyachkova, Y. G. Zainulin, M. Mashkovtsev, G. Yakovlev, and A. S. Vagapov, AIP Conf. Proc. **2015**, 020039 (2018).

26. V. Kortov, S. Zvonarev, A. Kiryakov, and D. Ananchenko, Mater. Chem. Phys. **170**, 168 (2016).

27. Ch. P. Poole, Jr., *Electron Spin Resonance: A Comprehensive Treatise on Experimental Techniques* (Dover, New York, 1997).

28. F. Méducin, S. A. Redfern, Y. Le Godec, H. J. Stone, M. G. Tucker, M. T. Dove, and W. G. Marshall, Am. Mineral. **89**, 981 (2004).

29. N. B. Hannay and C. P. Smyth, J. Am. Chem. Soc. **68**, 171 (1946).

30. F. W. Breivogel, Jr. and V. Sarkissian, J. Chem. Phys. **48**, 2442 (1968).

Translated by N. Saetova